

## MAJOR PAPER

# Numerical Experiments on the Contrast Capability of Magnetic Resonance Electrical Property Tomography

Song Duan<sup>1</sup>, Yurong Zhu<sup>2</sup>, Feng Liu<sup>3</sup>, and Sherman Xuegang Xin<sup>4\*</sup>

**Purpose:** Magnetic resonance electrical property tomography (MR EPT) is a technique for non-invasively obtaining the electric property (EP) distribution of biological tissues, with a promising potential for application in the early detection of tumors. However, the contrast capability (CC) of this technique has not been fully studied. This work aims to theoretically explore the CC for detecting the variation of EP values and the size of the imaging region.

**Methods:** A simulation scheme was specifically designed to evaluate the CC of MR EPT. The simulation study has the advantage that the magnetic field can be accurately obtained. EP maps of the designed phantom embedded with target regions of designated various sizes and EPs were reconstructed using the homogeneous Helmholtz equation based on  $B_1^+$  with different signal-to-noise ratios (SNRs). The CC was estimated by determining the smallest detectable EP contrast when the target region size was as large as the Laplacian kernel and the smallest detectable target region size when the EP contrast was the same as the difference between healthy and malignant tissues in the brain, based on the reconstructed EP maps.

**Results:** Using noise free  $B_1^+$ , the smallest detectable contrast  $\sigma$  and contrast  $\varepsilon_r$  were 1% and 3%, respectively, and the smallest detectable target region size was 1 mesh unit (the base unit size used in the simulation) for conductivity and relative permittivity. The smallest detectable EP contrast and target region size were decreased as the  $B_1^+$  SNR increased.

**Conclusion:** The CC of MR EPT was related with the SNR of the magnetic field. A small EP contrast and size were necessary for detection at a high-SNR magnetic field. Obtaining a high-SNR magnetic field is important for improving the CC of MR EPT.

**Keywords:** *contrast capability, electromagnetic simulation, magnetic resonance electrical property tomography, signal-to-noise ratio*

## Introduction

Electrical properties (EP) of biological tissues, including conductivity ( $\sigma$ ) and relative permittivity ( $\varepsilon_r$ ), have been the subject of research for several years.<sup>1–7</sup> Numerous studies have been conducted on the measurement of the EP values of various malignant and healthy tissue types at radiofrequency

(RF) and microwave frequency.<sup>1–5,8,9</sup> These investigations have consistently demonstrated that the EP values of malignant tissues have definite levels of difference compared with those of healthy tissues. Numerous factors, including relative intracellular and extracellular fluid volumes, ionic concentrations, and cellular membrane permeability, account for the difference mechanism of EP values between malignant and healthy tissues.<sup>1,2,10</sup> Considerable differences in EP values of even up to 577% may exist between malignant and healthy tissues.<sup>7</sup> Considering the biological continuous process of the alteration in EP values of tissues, we can assume that only a small change of EP values, for example, only 1%, occurs at the early stage of the progressive process of tissues developed from healthy to malignant status.<sup>11</sup> Given the large contrast gap of EP values between healthy and malignant tissues, people believe that detecting the variations in EP values of tissues at the beginning of the entire progressive process from healthy to malignant status may be beneficial for the early detection of tumors.<sup>12–14</sup>

<sup>1</sup>Department of Radiation Oncology, Sun Yat-sen Memorial Hospital, Sun Yat-sen University, Guangdong, China

<sup>2</sup>Department of Biomedical Engineering, Southern Medical University, Guangdong, China

<sup>3</sup>School of Information Technology and Electrical Engineering, University of Queensland, Qld, Australia

<sup>4</sup>School of Medicine, South China University of Technology, Guangzhou Higher Education Mega Centre, Panyu District, Guangzhou, Guangdong 510006, China

\*Corresponding author, Phone: +86-020-39381185, E-mail: xinxs@scut.edu.cn

©2019 Japanese Society for Magnetic Resonance in Medicine

This work is licensed under a Creative Commons Attribution-NonCommercial-NoDerivatives International License.

Received: December 6, 2018 | Accepted: March 14, 2019

Although the knowledge on EP values of tissues can be easily obtained *in vitro*, for example, using the open-ended coaxial probe method,<sup>10,15</sup> non-invasively obtaining the tomographic EP data *in vivo* is difficult until the technique magnetic resonance electrical property tomography (MR EPT) was proposed. On the basis of the measurement of the transmitted  $B_1^+$  field of the MRI system at the Larmor frequency,<sup>16–20</sup> MR EPT can image the EP distribution inside the human body without requiring a current injection, as implemented in electric impedance tomography (EIT)<sup>21</sup> and magnetic resonance EIT.<sup>22,23</sup> The measurement mechanism is in the  $B_1^+$  field being electromagnetically distorted by the loaded human body. Therefore, the quantitative assessment of the distorted  $B_1^+$  allows the inverse reconstruction of the EP values of tissues. The concept of EP imaging was first introduced by Haacke et al.<sup>24</sup> and was applied practically by Wen et al.<sup>25</sup> Wen et al.<sup>25</sup> indicated that the distribution of the RF field in high-field MRI directly correlates with the EP distributions in the sample and that the relationship between the RF field and EP can be explained by a simplified EPT reconstruction equation, that is, the homogeneous Helmholtz equation. Since its proposal by Wen et al.,<sup>25</sup> this simplified EPT reconstruction equation has become the most popular algorithm applied in the majority of EPT studies.<sup>14,26–33</sup> In recent years, numerous studies have focused on the capability of the MR EPT technique. For example, in prior work, the validity of homogeneous Helmholtz equation was investigated by Seo et al.,<sup>33</sup> demonstrating that a large reconstruction error occurred in inhomogeneous objects in which the EP homogenous assumption in the homogeneous Helmholtz equation fails. An alternative study conducted by Lee et al.<sup>34</sup> discussed the limit of signal-to-noise ratio (SNR) using a homogenous phantom, and it showed that the SNR of reconstructed EP is proportional to the square of the linear dimension of the ROI over which the EPs are determined and to the square root of the number of voxels in the ROI. Duan et al.<sup>14</sup> quantitatively analyzed the reconstruction errors of Helmholtz-based MR EPT at the interfaces of adjacent tissues, showing the limitation of this homogeneous Helmholtz equation when applied to the human body. Mandija et al.<sup>35</sup> indicated that numerical error is a major cause of limited accuracy in Helmholtz-based MR-EPT reconstructions. These studies have shown the various limitations of Helmholtz-based MR EPT in EP reconstruction, especially for inhomogeneous objects. Such limitations can lead to problems when the MR EPT algorithm is applied *in vivo*. For example, when the MR EPT is applied for the early detection of tumors that have different EP values with surrounding tissues, the detection of lesions may be affected due to the limitations of this technique. This question highlights the importance of the research on the contrast capability (CC) of MR EPT, i.e., the detection capability on the variation in EP values of tissues and the size of the image region. Wang et al.<sup>36</sup> evaluated the sensitivity for structures of various EP values and geometrical sizes at 7T for a boundary-informed electrical property tomography technique that can reliably retrieve EP distributions inside an

object using an external EP reference area. However, to our knowledge, the CC of MR EPT remains unexplored.

This study aims to investigate the CC of MR EPT using the homogeneous Helmholtz equation. Hence, the reconstruction of MR EPT is required, and obtaining the  $B_1^+$  data is the first step. However, in the practical MR scan, the  $B_1^+$  data inevitably involves engineering artifacts, such as Gibbs ringing that occurs when the spatial resolution is insufficient to represent small structures in the object<sup>37</sup> and the distortion or blurring caused by resonance offsets and hardware limitations<sup>38</sup>; in addition, the presently available  $B_1$  mapping methods in engineering cannot obtain the phase map of the  $B_1^+$  field.<sup>39–41</sup> In practice, a rough approximation of transmit phase was obtained by the transceive phase assumption using a quadrature volume coil.<sup>27,39,40,42</sup> On the contrary, accurately obtaining the full set of  $B_1^+$  data using numerical electromagnetic simulation is easy. Therefore, in this work, the CC of MR EPT was theoretically investigated via numerical simulation. A carefully designed simulation scheme was utilized to obtain the  $B_1^+$  data of a designed dielectric model embedded with a series of target regions with various sizes and EP values. The EP distributions were reconstructed using the homogeneous Helmholtz equation based on the obtained  $B_1^+$  with different SNR. The smallest detectable EP contrast (when the target region size was as large as the Laplacian kernel) and smallest detectable target region size (when the EP contrast was the same as the difference between healthy and malignant tissues in the brain) were determined following the reconstructed EP maps and used to describe the CC of MR EPT.

## Materials and Methods

### Modeling

In this study, a numerical simulation was carefully designed to obtain  $B_1^+$  field distribution as the base for analyzing the CC of MR EPT. Simulations were performed on a commercial simulation software (SEMCAD X. 14.6, Schmid & Partner Engineering AG, Zurich, Switzerland), which considered a transmit coil loaded with a dielectric model, as shown in Fig. 1.

The transmit coil was a 16-leg, 3T high-pass birdcage coil. In the coil setup, the coil leg length was 40 cm and the diameter of the end-ring was 30 cm. A total of 16 capacitors were distributed on each end-ring with equal space having a uniform capacitance of 16.22 pF. Each leg had a unit amplitude current source at the center, and all sources had the same current direction. From leg to leg, the phases of the current sources were assigned with a step increment of  $2\pi/16$ .

A dielectric cube (referred to as the background cube) was constructed in the SEMCAD, which was considered for the side length of 25 mesh units (1 mesh unit was equal to the side length of a given isotropic voxel size). A small cubic target region was set in the center of the background cube, as shown in Fig. 1. The EP of background cube was the same as

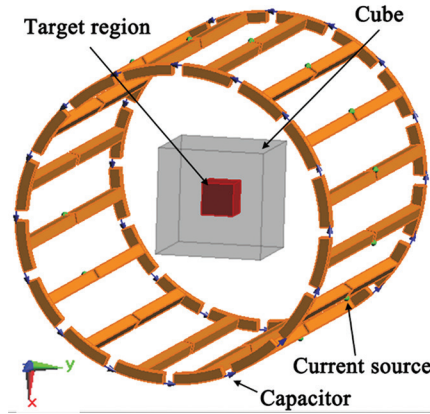


**Fig. 1** Photographs of the high-pass birdcage coil loaded with the dielectric cube model that embedded a cubic target region in its center. The background cube (grey), target region (red), current source (green), and capacitor (blue) are shown using black arrows. The co-ordinate system at the bottom left shows the  $x$ -,  $y$ -, and  $z$ -directions.

that of healthy white matter ( $\sigma = 0.3421$  S/m and  $\epsilon_r = 52.53$ ).<sup>1-3</sup> To investigate the detection capability of MR EPT on the variation in EP values of tissues and the size of the image region, different EPs and sizes were assigned to the target region. The details of the simulation settings of the target region are as follows.

In the investigation of the detection capability on the variation in EP values of tissues, various EP values were assigned to the target region, thereby forming the following pairs of ( $\text{contrast}_\sigma$ ,  $\text{contrast}_{\epsilon_r}$ ): (0.01:0.02:1.01, 0) and (0, 0.01:0.02:0.27), where  $\text{contrast}_\sigma$  and  $\text{contrast}_{\epsilon_r}$  are the contrasts of conductivity and relative permittivity, respectively, and are calculated as Eqs. [1] and [2]:

$$\text{contrast}_\sigma = \frac{\sigma_{\text{TR}} - \sigma_{\text{B}}}{\sigma_{\text{B}}}, \quad [1]$$

$$\text{contrast}_{\epsilon_r} = \frac{\epsilon_{r\text{TR}} - \epsilon_{r\text{B}}}{\epsilon_{r\text{B}}}, \quad [2]$$

where  $\sigma_{\text{TR}}$  and  $\epsilon_{r\text{TR}}$  represent the conductivity and relative permittivity of the target region and  $\sigma_{\text{B}}$  and  $\epsilon_{r\text{B}}$  denote the conductivity and relative permittivity of the background cube, respectively. The detection capability on the variation of conductivity and relative permittivity was studied separately. When the detection capability on the variation of conductivity was investigated,  $\text{contrast}_\sigma$  was increased from 0.01 to 1.01, and  $\text{contrast}_{\epsilon_r}$  was fixed at 0, i.e., the target region has the same  $\epsilon_r$  as the background cube. Similarly, when the detection capability on the variation of relative permittivity was investigated,  $\text{contrast}_{\epsilon_r}$  was increased from 0.01 to 0.27, and  $\text{contrast}_\sigma$  was fixed at 0. The smallest investigated  $\text{contrast}_{\text{EP}}$  was set as 1%, which is small compared with the large difference (even up to 577%) in EP values between the normal and malignant tissues.<sup>7,43</sup> The  $\text{contrast}_{\text{EP}}$  smaller than 1% was not studied here. The maximum  $\text{contrast}_{\text{EP}}$

investigated was equal to the contrast between the human glioma and healthy white matter.<sup>1-3,43</sup> The side length of the target region was set as 7 mesh units; thus, the target region was as large as the Laplacian kernel used in this study, which is the smallest size of image region meeting the assumption “locally constant EP” in the homogenous Helmholtz equation.

In the investigation of the detection capability on the size of the image region, the target region was constructed with a side length of 1–10 mesh units and EP values equal to human glioma ( $\sigma = 0.6836$  S/m,  $\epsilon_r = 66.18$ ).<sup>43</sup>

### Generation of magnetic field

The built model was positioned at the center of the birdcage coil. The voxel size in the region of the phantom was set as  $1 \times 1 \times 1$  mm<sup>3</sup>, which was a recommended voxel size for MR image acquisition, considering scan time and image quality.<sup>44</sup> After the SEMCAD simulation,  $B_1^+$  data of the model were exported into MATLAB (MathWorks, Natick, MA, USA) for further processing. To observe the changes in magnitude and phase in the target region, the magnitude and phase maps were normalized by the magnitude and phase maps generated using a homogenous model in which the EP of target region was equal to background cube, i.e., the EP values of the background cube and target region were equal to the EP of the healthy white matter. The normalized magnitude and phase maps across the center of the target region were presented. In practical measurement, the data of magnetic fields are consistently polluted by noise. In this manuscript, the measurement noise was included by adding complex Gaussian noise with zero mean to the  $B_1^+$  field, thereby forming several SNR levels of  $B_1^+$  magnitude in the range of

60 to  $+\infty$ . The SNR was defined as  $\text{SNR} = 20 \log_{10} \frac{|B_1^+|}{|N|}$ ,

where  $B_1^+$  is the simulated data and  $N$  denotes the Gaussian noise added in the simulated  $B_1^+$ .

### Reconstruction of EP

After the  $B_1^+$  of the model was obtained, the EP distributions of the dielectric model were reconstructed using the following homogeneous Helmholtz equation [3]<sup>25</sup>:

$$\kappa = \frac{-\nabla^2 B_1^+}{\omega^2 \mu B_1^+}, \quad [3]$$

where  $\omega$  is angular frequency and  $\kappa = \epsilon - i \frac{\sigma}{\omega}$  represents

the complex permittivity and is assumed to be isotropic.  $\mu$  denotes the magnetic permeability. In the human body,  $\mu$  was assumed to be constant and equal to the magnetic permeability of the free space  $\mu_0 = 4\pi \times 10^{-7}$ . By separating the real and imaginary components of Eq. [3], conductivity  $\sigma$  and relative permittivity  $\epsilon_r$  can be computed as

$$\sigma = \frac{1}{\omega \mu} \text{Im} \left\{ \frac{\nabla^2 B_1^+}{B_1^+} \right\}, \quad [4]$$

$$\varepsilon_r = \frac{-1}{\omega^2 \mu \varepsilon_0} \operatorname{Re} \left\{ \frac{\nabla^2 B_1^+}{B_1^+} \right\}, \quad [5]$$

where  $\varepsilon_0 = 8.8542 \times 10^{-12}$  F/M refers to the free space permittivity. The numerical Laplacian calculation in Eqs. [4] and [5] was realized using the Savitzky–Golay kernel ( $K_{SG}$ ).<sup>45,46</sup> The applied  $K_{SG}$  was as following Eqs. [6] and [7]:

$$\text{Kernel}_{\text{small},i} = \left\{ 2^{-|i-2|} \begin{bmatrix} 1 & -\frac{1}{2} & -1 & -\frac{1}{2} & 1 \\ 2 & -1 & -2 & -1 & 2 \\ 1 & -\frac{1}{2} & -1 & -\frac{1}{2} & 1 \end{bmatrix} \right\}_{i=1,2,3}, \quad [6]$$

$$\text{Kernel}_{\text{large},i} = \left\{ 2^{-|i-2|} \begin{bmatrix} \frac{5}{2} & 0 & \frac{-3}{2} & -2 & \frac{-3}{2} & 0 & \frac{5}{2} \\ 5 & 0 & -3 & -4 & -3 & 0 & 5 \\ \frac{5}{2} & 0 & \frac{-3}{2} & -2 & \frac{-3}{2} & 0 & \frac{5}{2} \end{bmatrix} \right\}_{i=1,2,3}, \quad [7]$$

where the index  $i$  indicates the third dimension of the small ( $5 \times 3 \times 3$ ,  $\text{Kernel}_{\text{small}}$ ) and large ( $7 \times 3 \times 3$ ,  $\text{Kernel}_{\text{large}}$ ) kernels. These two kernels were used to calculate the second-order derivatives of the target voxel in the  $x$ ,  $y$ , and  $z$ -directions; summing the results of the three derivatives results in the Laplacian kernel. The  $7 \times 3 \times 3$  and  $5 \times 3 \times 3$  kernels were used for in- and inter-plane computations, respectively. In the inter-plane direction, a smaller kernel was selected to reduce the number of slices required for reconstruction, thereby decreasing the measurement time.

### Evaluation of CC

The CC evaluation was based on the reconstructed EP maps. The designated target region is detectable if the mean EP of the target region ( $\overline{\text{EP}}_{\text{TR}}$ ), the mean EP of the background ( $\overline{\text{EP}}_{\text{B}}$ ), and the standard deviation of the EP of the background ( $\text{STD}_{\text{B,EP}}$ ) satisfied the following relation [8]:

$$\overline{\text{EP}}_{\text{TR}} - \overline{\text{EP}}_{\text{B}} > \text{STD}_{\text{B,EP}}. \quad [8]$$

The smallest detectable contrast $_{\text{EP}}$  (when the target region was as large as the Laplacian kernel) and smallest detectable target region size (when the EP of target region was equal to glioma) were determined and used to describe the CC.

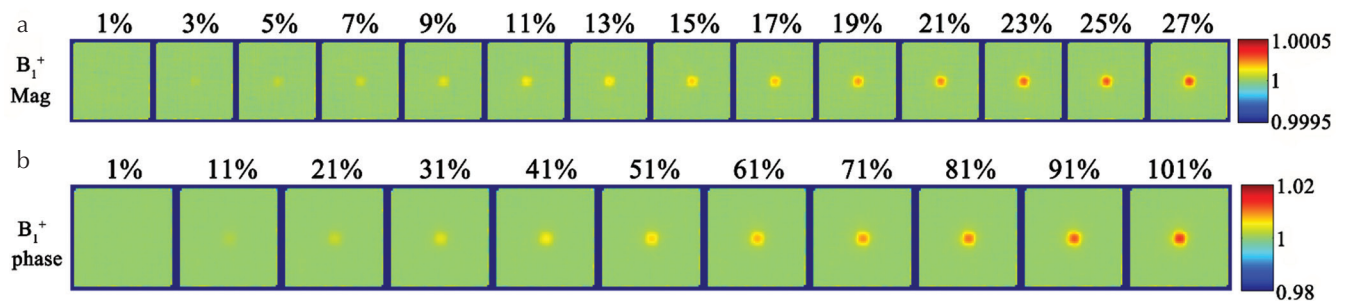
## Results

### Detection capability on the variation of EP

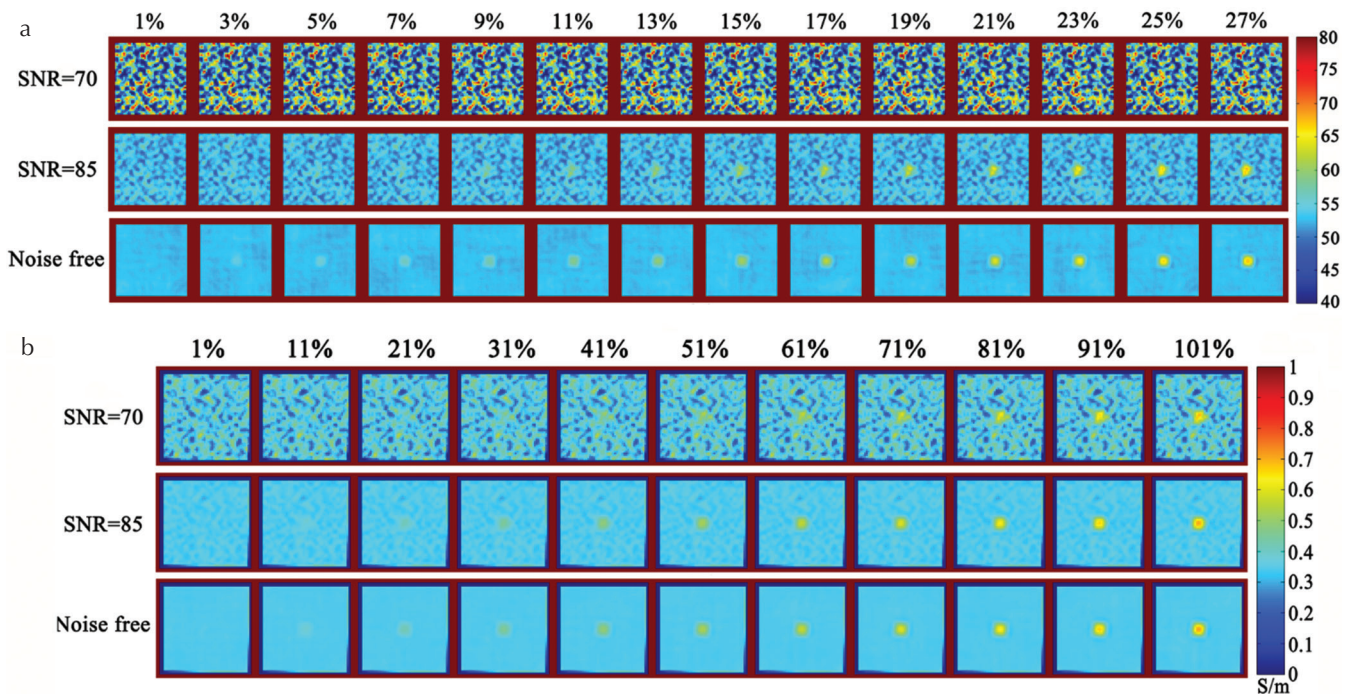
The investigation of the detection capability on the variation of EP was conducted using a target region with fixed size and varied EP. The size of the target region was approximately the size of the Laplacian kernel used for the EP reconstruction. The  $B_1^+$  data of the built model were generated using the above-described numerical simulation procedure. Fig. 2 shows the transverse distributions of normalized magnitude and phase across the central area of the target region, in which Fig. 2a illustrates the normalized magnitude maps with respect to the contrast $_{\varepsilon_r}$  1–27% (corresponding to the first to the last column, respectively). Fig. 2b presents the normalized phase maps with respect to the contrast $_{\varepsilon_r}$  1 to 101%. The normalized magnitude and phase in the target region were increased with contrast $_{\varepsilon_r}$  and contrast $_{\sigma}$ .

Figure 3 displays the reconstructed EP distributions of the built model across the center of the target region for the contrast $_{\sigma}$  from 1 to 101%, and the contrast $_{\varepsilon_r}$  from 1 to 27%, when the  $B_1^+$  SNR was 70, 85, and  $+\infty$  (noise free). The conductivity and relative permittivity over the target region were increased with contrast $_{\sigma}$  and contrast $_{\varepsilon_r}$ , respectively. With the decrease in SNR, the target region disappeared in the reconstructed EP maps, especially for the target regions with small contrast $_{\text{EP}}$ .

Figure 4 plots the smallest detectable contrast $_{\text{EP}}$  for different  $B_1^+$  SNRs. When the noise free  $B_1^+$  data were used, the smallest detectable contrast $_{\sigma}$  and contrast $_{\varepsilon_r}$  were as small as 1% and 3%, respectively. The smallest detectable contrast $_{\text{EP}}$  was decreased as the SNR of  $B_1^+$  data was increased.



**Fig. 2** Transverse distributions of normalized magnitude and phase across the center of the target region for different contrast $_{\text{EP}}$  values. The size of the target region was approximately the size of the Laplacian kernel used for the electric property (EP) reconstruction. (a) Normalized magnitude maps in which contrast $_{\varepsilon_r}$  was increased from 1% to 27%, corresponding to the first to the last column. (b) Normalized phase maps in which contrast $_{\sigma}$  was increased from 1 to 101%.



**Fig. 3** Reconstructed electric property (EP) distributions of the constructed model across the center of the target region. (a) Reconstructed relative permittivity maps. From the first to the last columns, contrast<sub>ε</sub> was from 1% to 27%. From the first to the third rows, the  $B_1^+$  SNRs were 70, 85, and  $+\infty$  (noise free), respectively. (b) Reconstructed conductivity maps. From the first to the last columns, the contrast<sub>σ</sub> values were 1–101%. From the first to the third rows, the  $B_1^+$  SNRs were 70, 85, and  $+\infty$ , respectively. SNR, signal-to-noise ratio.

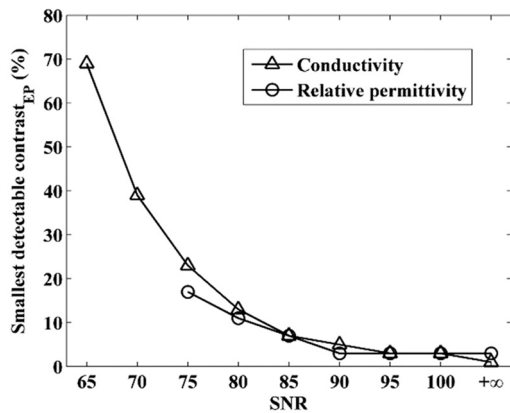


**Fig. 4** Smallest detectable contrast<sub>ε</sub> (triangle) and contrast<sub>σ</sub> (circle) for different  $B_1^+$  SNRs. SNR =  $+\infty$  indicates that no gauss noise was added to the simulated  $B_1^+$  data. The smallest detectable contrast<sub>EP</sub> was decreased as the SNR of  $B_1^+$  data was increased. The target regions cannot be detected in the investigated range of electric property (EP) contrast on the basis of the reconstructed conductivity and relative permittivity maps, when the SNRs were smaller than 65 and 75, respectively. SNR, signal-to-noise ratio.

The target regions cannot be detected in the investigated range of EP contrast when the SNR smaller than 65 and 75, respectively.

#### Detection capability on the size of the image region

The detection capability on the size of the image region was investigated using a target region with fixed EP and varied size.

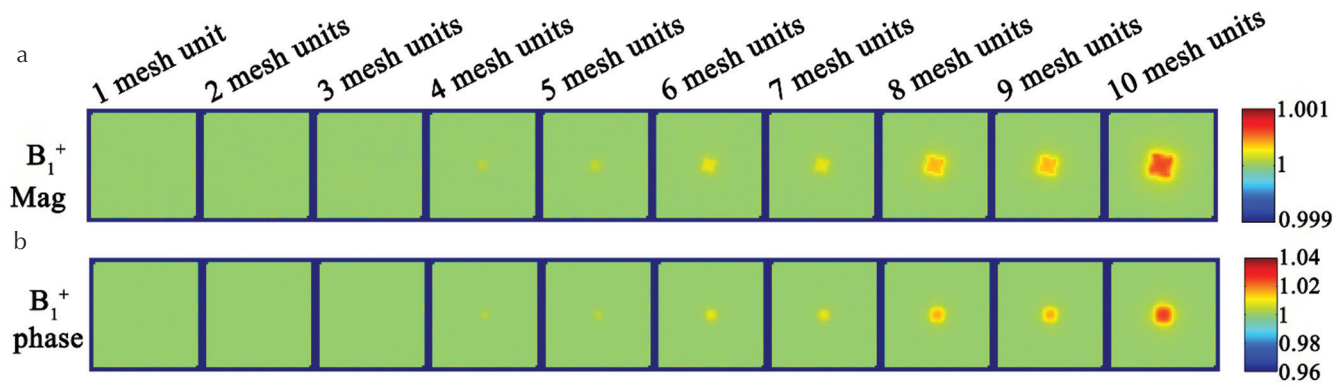
The assigned EP values of target region were the same as the EP of human glioma. Figure 5 presents the transverse distributions of normalized magnitude and phase across the central area of the target region for different target region sizes (side lengths from 1 to 10 mesh units). The normalized magnitude and phase in the target region were increased with the target region size.

Figure 6 presents the reconstructed EP distributions of the built model across the center of the target region for a size of 1–10 mesh units, when the  $B_1^+$  SNR was 70, 85, and  $+\infty$  (noise free). The reconstructed EP over the target region is decreased as the target region size decreases. With the decrease in SNR, the target region disappeared in the reconstructed EP maps, especially for the target regions with small size.

Figure 7 plots the smallest detectable target region size for different  $B_1^+$  SNRs. When the noise free  $B_1^+$  data were used, the smallest detectable target region size was 1 mesh unit for conductivity and relative permittivity. The smallest detectable target region size decreased as the SNR of  $B_1^+$  was increased. The target regions cannot be detected in the investigated range of target region size when the SNRs were smaller than 65 and 70, respectively.

## Discussion

Given the existence of a large difference in EPs between benign and malignant tissues, the technique of MR EPT may



**Fig. 5** Transverse distributions of normalized magnitude (a) and phase (b) across the central area of the target region for different target region sizes. The electric property (EP) values of the target region and background were the same as those for human glioma and healthy grey matter, respectively. From the first to the last columns, the side length of the target region was increased from 1 to 10 mesh units.

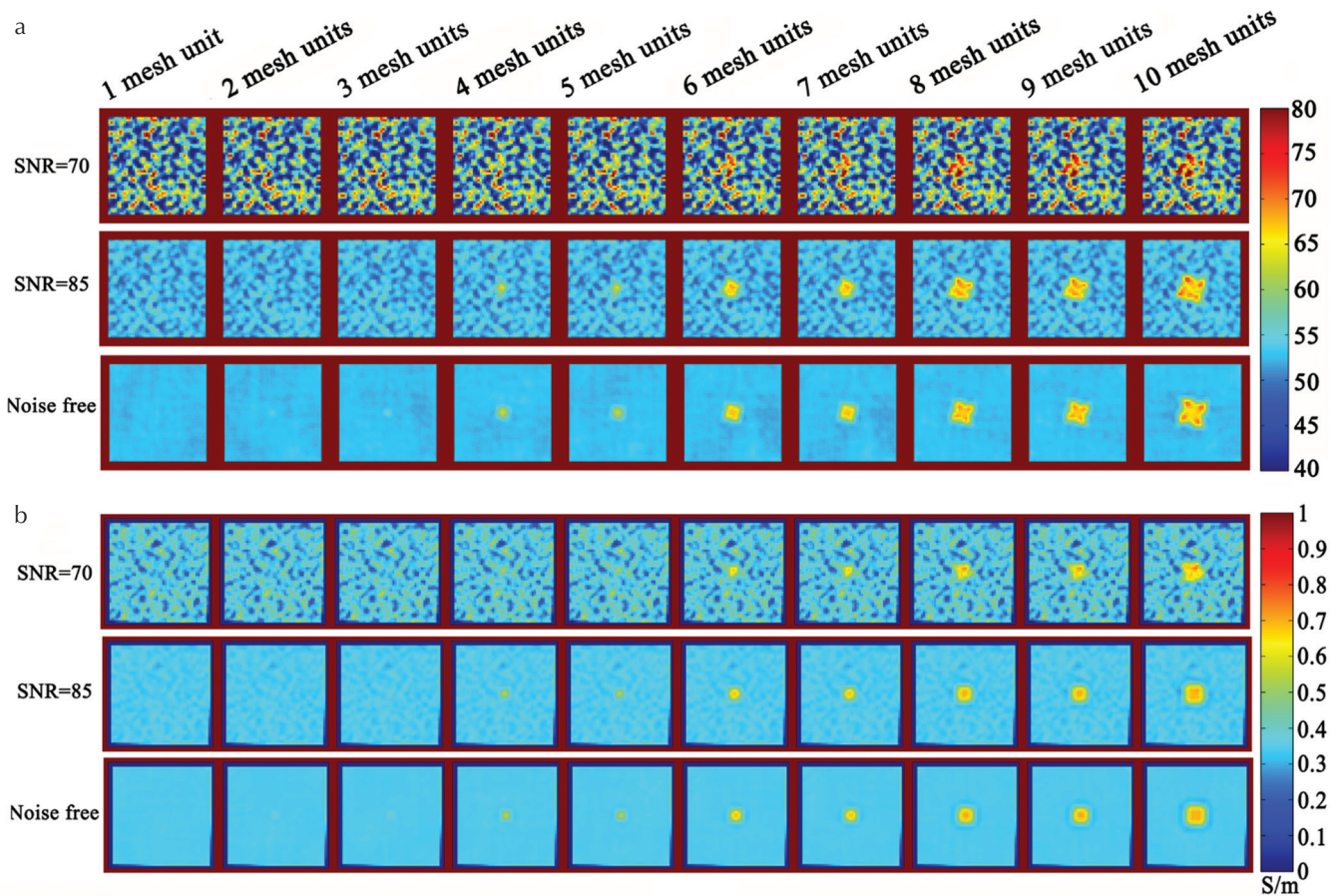


**Fig. 6** Reconstructed relative permittivity (a) and conductivity (b) distributions of the constructed model across the center of the target region. From the first to the last columns, the side lengths of the target region were 1–10 mesh units, respectively. From the first to the third rows in (a) and (b), the  $B_1^+$  SNRs were 70, 85, and  $+\infty$  (noise free), respectively. SNR, signal-to-noise ratio.

be valuable for the early clinical detection of tumors. The current manuscript focused on the CC of MR EPT, which is meaningful for the application of this technique. The CC of MR EPT was determined at a frequency of 128 MHz on the basis of the homogeneous Helmholtz equation.

Two central challenges of EPT are the boundary issue, in which severe reconstruction error of EP can occur at the interfaces of adjacent tissues with different EP,<sup>14,33</sup> and the transmit phase, which is difficult to determine exactly.<sup>40</sup> Certain strategies have been proposed to resolve

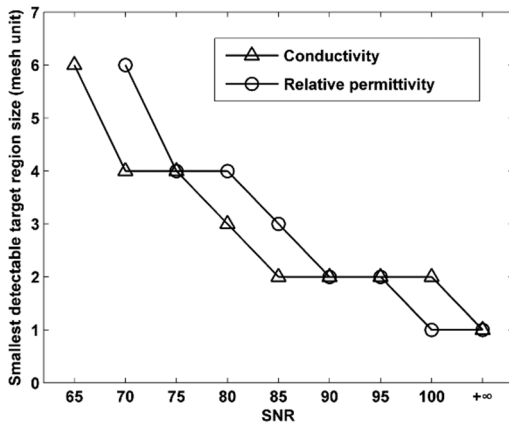


**Fig. 7** Smallest detectable target region size determined on the basis of reconstructed relative permittivity (circle) and conductivity (triangle) maps, for different  $B_1^+$  SNRs. The smallest detectable target region size is decreased as the SNR of  $B_1^+$  data was increased. The target regions cannot be detected in the investigated range of target region size on the basis of the reconstructed conductivity and relative permittivity maps when the SNRs were smaller than 65 and 70, respectively. SNR, signal-to-noise ratio.

such challenges.<sup>29,47–50</sup> Some of the newly proposed EPT reconstruction methods involve the dual-excitation algorithm,<sup>48</sup> convection–reaction equation-based MR EPT,<sup>51</sup> gradient-based EPT,<sup>52</sup> contrast source inversion-EPT,<sup>53</sup> and water content-based EPT.<sup>12</sup> These approaches were implemented by rewriting the Helmholtz equation combined with some approximations or prior knowledge. In comparison with the abovementioned approaches, the homogeneous Helmholtz equation is a basic reconstruction formulation derived directly from the Helmholtz equation. Therefore, using the basic reconstruction formulation to indicate the basic characteristics of the CC of MR EPT is reasonable.

A carefully designed numerical simulation strategy was used to obtain  $B_1^+$ . The different changes in magnitude and phase of  $B_1^+$  were observed for different target regions. The changes were related to the alterations of the EP and size of the target region. As shown in Figs. 2 and 5, the normalized magnitude and phase over the target regions increased with the increase of the geometric volume of the target region and contrast<sub>EP</sub>. These results indicated that the influence of the target region on the magnetic field was increased with the increase in the size and EP of the target region. Thus, a large difference in reconstructed EP was observed between the target region and background cube for these cases with larger contrast<sub>EP</sub> and target region size, as shown in Figs. 3 and 6.

Determining the smallest detectable contrast<sub>EP</sub> at different target region sizes and the smallest detectable target region sizes at different contrast<sub>EP</sub> values is complicated because of the numerous cases of size and contrast<sub>EP</sub> in the target region. In this study, the CC of MR EPT was evaluated by determining the smallest detectable contrast<sub>EP</sub> (when the

target region was as large as the Laplacian kernel) and smallest detectable target region size (when the EP of target region was equal to glioma), based on the reconstructed EP maps. When the noise free  $B_1^+$  data were used, the smallest detectable contrast<sub>EP</sub> was 1% for conductivity and 3% for relative permittivity, and the smallest detectable target region size was 1 mesh unit for conductivity and relative permittivity. The smallest detectable contrast<sub>EP</sub> and smallest detectable target region size were increased as the  $B_1^+$  SNR declined, as shown in Figs. 4 and 7. This trend can also be observed in Figs. 3 and 6, where the target regions with small contrast<sub>EP</sub> and size disappeared when the  $B_1^+$  SNR was lower. Therefore, small EP contrast and size were necessary for detecting the imaging region at high SNRs of the magnetic field. Obtaining the high-SNR magnetic field data is important for improving the CC of MR EPT.

Image noise is an undesirable component correlated with the desired signal, which is consistently contained in practical measurement.<sup>54</sup> In this study, the influence of image noise on the CC of MR EPT was considered by adding complex Gaussian noise in the simulated  $B_1^+$  data. The target regions with small size and contrast<sub>EP</sub> are sensitive to image noise. These target regions were undetectable even when small noise was added. In the MR scanning, the image noise is related to numerous parameters,<sup>55</sup> such as physical and instrumental parameters including the strength of the main field  $B_0$ , the random electrical fluctuations associated with the resistances of the receiver coil and the body, and the imaging sequence parameters, e.g., the excitation tip angles, sequence timing, and data acquisition time. During the implementation of the MR EPT, these parameters will affect the SNR of the  $B_1^+$  data and finally affect the CC of the technique.

Previous studies<sup>35,42</sup> indicate that a small Laplacian kernel leads to spatially limited numerical boundary errors, which will be ideal for convoluted tissue structures, such as the human brain. However, in reality, the acquired images are intrinsically affected by local fluctuations, such as those from thermal noise. Small kernels are highly sensitive to local signal noise. To minimize the effect of spatial fluctuations, relatively large Laplacian kernel in combination with Gaussian apodization, such as the van Lier's kernel<sup>28</sup> and  $K_{SG}$ ,<sup>45,46</sup> was often adopted. Furthermore, Lee et al.<sup>34</sup> showed that the  $K_{SG}$  is optimal for noise reduction. Therefore, the  $K_{SG}$  was selected in the current study to reconstruct the EP distribution of the model.

This manuscript only focused on the frequency of 128 MHz, which is the most widely available frequency. The CC of MR EPT at other frequencies should be different from the results presented in this study because the SNR of the obtained magnetic field and the local field curvature (positively correlated to tissue EPs) varied with the applied frequency, leading to different noise levels in the reconstructed EP.

## Conclusion

The CC of the MR EPT technique was related to the SNR of magnetic fields. Small EP contrast and size were necessary for detection at high SNR of the magnetic field. Obtaining high-SNR magnetic field data is important for improving the CC of MR EPT.

## Funding

This study was partially supported by the National Natural Science Foundation of China (grant number 61671229), Science and Technology Program of Guangdong, China (No. 2017B020229004), Science and Technology Program of Guangzhou, China (No. 201704020091), and National Key Research and Development Program of China (No. 2016YFC0100800, 2016YFC0100801, 2016YFC0100802).

## Conflicts of Interest

The authors declare that they have no conflicts of interest.

## References

- Gabriel C, Gabriel S, Corthout E. The dielectric properties of biological tissues: I. Literature survey. *Phys Med Biol* 1996; 41:2231–2249.
- Gabriel S, Lau RW, Gabriel C. The dielectric properties of biological tissues: II. Measurements in the frequency range 10 Hz to 20 GHz. *Phys Med Biol* 1996; 41:2251–2269.
- Gabriel S, Lau RW, Gabriel C. The dielectric properties of biological tissues: III. Parametric models for the dielectric spectrum of tissues. *Phys Med Biol* 1996; 41:2271–2293.
- Chaudhary SS, Mishra RK, Swarup A, Thomas JM. Dielectric properties of normal & malignant human breast tissues at radiowave & microwave frequencies. *Indian J Biochem Biophys* 1984; 21:76–79.
- Surowiec AJ, Stuchly SS, Barr JB, Swarup A. Dielectric properties of breast carcinoma and the surrounding tissues. *IEEE Trans Biomed Eng* 1988; 35:257–263.
- Foster KR, Schwan HP. Dielectric properties of tissues and biological materials: a critical review. *Crit Rev Biomed Eng* 1989; 17:25–104.
- Joines WT, Zhang Y, Li C, Jirtle RL. The measured electrical properties of normal and malignant human tissues from 50 to 900 MHz. *Med Phys* 1994; 21:547–550.
- Kim SY, Shin J, Kim DH, et al. Correlation between conductivity and prognostic factors in invasive breast cancer using magnetic resonance electric properties tomography (MREPT). *Eur Radiol* 2016; 26:2317–2326.
- Tha KK, Katscher U, Stehning C, et al. Electrical conductivity characteristics of meningiomas: noninvasive assessment using electric properties tomography. *Proceedings of the 23rd Annual Meeting ISMRM, Toronto, 2015*; 4397.
- Li Z, Deng G, Li Z, et al. A large-scale measurement of dielectric properties of normal and malignant colorectal tissues obtained from cancer surgeries at Larmor frequencies. *Med Phys* 2016; 43:5991–5997.
- Li Z, Wang W, Cai Z, et al. Variation in the dielectric properties of freshly excised colorectal cancerous tissues at different tumor stages. *Bioelectromagnetics* 2017; 38: 522–532.
- Michel E, Hernandez D, Lee SY. Electrical conductivity and permittivity maps of brain tissues derived from water content based on T<sub>1</sub>-weighted acquisition. *Magn Reson Med* 2017; 77:1094–1103.
- Li C, Yu W, Huang SY. An MR-based viscosity-type regularization method for electrical property tomography. *Tomography* 2017; 3:50–59.
- Duan S, Xu C, Deng G, Wang J, Liu F, Xin SX. Quantitative analysis of the reconstruction errors of the currently popular algorithm of magnetic resonance electrical property tomography at the interfaces of adjacent tissues. *NMR Biomed* 2016; 29:744–750.
- Fu F, Xin SX, Chen W. Temperature- and frequency-dependent dielectric properties of biological tissues within the temperature and frequency ranges typically used for magnetic resonance imaging-guided focused ultrasound surgery. *Int J Hyperthermia* 2014; 30:56–65.
- Akoka S, Franconi F, Seguin F, Le Pape A. Radiofrequency map of an NMR coil by imaging. *Magn Reson Imaging* 1993; 11:437–441.
- Collins CM, Yang QX, Wang JH, et al. Different excitation and reception distributions with a single-loop transmit-receive surface coil near a head-sized spherical phantom at 300 MHz. *Magn Reson Med* 2002; 47:1026–1028.
- Van de Moortele PF, Akgun C, Adriany G, et al. B<sub>1</sub> destructive interferences and spatial phase patterns at 7 T with a head transceiver array coil. *Magn Reson Med* 2005; 54:1503–1518.
- Stollberger R, Wach P. Imaging of the active B<sub>1</sub> field *in vivo*. *Magn Reson Med* 1996; 35:246–251.
- Wang J, Qiu M, Yang QX, Smith MB, Constable RT. Measurement and correction of transmitter and receiver induced nonuniformities *in vivo*. *Magn Reson Med* 2005; 53:408–417.
- Goncalves SI, de Munck JC, Verbunt JPA, Bijma F, Heethaar RM, Lopes da Silva F. *In vivo* measurement of the brain and skull resistivities using an EIT-based method and realistic models for the head. *IEEE Trans Biomed Eng* 2003; 50:754–767.
- İder YZ, Birgül Ö. Use of the magnetic field generated by the internal distribution of injected currents for electrical impedance tomography (MR-EIT). *Turk J Elec Eng & Comp Sci* 1998; 6:215–225.
- Seo JK, Kwon O, Woo EJ. Magnetic resonance electrical impedance tomography (MREIT): conductivity and current density imaging. *J Phys* 2005; 12:140–155.
- Haacke EM, Petropoulos LS, Nilges EW, Wu DH. Extraction of conductivity and permittivity using magnetic resonance imaging. *Phys Med Biol* 1991; 36:723–734.
- Wen H. Noninvasive quantitative mapping of conductivity and dielectric distributions using RF wave propagation effects in high-field MRI. *Proceedings of SPIE The International Society for Optical Engineering* 5030, San Diego, 2003; 471–477.
- Voigt T, Katscher U, Doessel O. Quantitative conductivity and permittivity imaging of the human brain using

- electric properties tomography. *Magn Reson Med* 2011; 66:456–466.
27. Katscher U, Voigt T, Findekle C, Vernickel P, Nehrke K, Dössel O. Determination of electric conductivity and local SAR via B<sub>1</sub> mapping. *IEEE Trans Med Imaging* 2009; 28:1365–1374.
  28. van Lier AL, Brunner DO, Pruessmann KP, et al. B<sub>1</sub><sup>+</sup> phase mapping at 7T and its application for in vivo electrical conductivity mapping. *Magn Reson Med* 2012; 67:552–561.
  29. Liu J, Zhang X, van de Moortele PF, Schmitter S, He B. Determining electrical properties based on B<sub>1</sub> fields measured in an MR scanner using a multi-channel transmit/receive coil: a general approach. *Phys Med Biol* 2013; 58:4395–4408.
  30. Michel E, Hernandez D, Cho MH, Lee SY. Denoising of B<sub>1</sub><sup>+</sup> field maps for noise-robust image reconstruction in electrical properties tomography. *Med Phys* 2014; 41:102304.
  31. Kim HJ, Jeong WC, Sajib SZ, et al. Simultaneous imaging of dual-frequency electrical conductivity using a combination of MREIT and MREPT. *Magn Reson Med* 2014; 71:200–208.
  32. Kim DH, Choi N, Gho SM, Shin J, Liu C. Simultaneous imaging of in vivo conductivity and susceptibility. *Magn Reson Med* 2014; 71:1144–1150.
  33. Seo JK, Kim MO, Lee J, et al. Error analysis of nonconstant admittivity for MR-based electric property imaging. *IEEE Trans Med Imaging* 2012; 31:430–437.
  34. Lee SK, Bulumulla S, Hancu I. Theoretical investigation of random noise-limited signal-to-noise ratio in MR-based electrical properties tomography. *IEEE Trans Med Imaging* 2015; 34:2220–2232.
  35. Mandija S, Sbrizzi A, Katscher U, Luijten PR, van den Berg CAT. Error analysis of helmholtz-based MR-electrical properties tomography. *Magn Reson Med* 2018; 80: 90–100.
  36. Wang Y, Shao Q, van de Moortele PF, et al. Mapping electrical properties heterogeneity of tumor using boundary informed electrical properties tomography (BIEPT) at 7T. *Magn Reson Med* 2019; 81:393–409.
  37. Bernstein MA, Huston J, Ward HA. Imaging artifacts at 3.0T. *J Magn Reson Imaging* 2006; 24:735–746.
  38. Smith TB, Nayak KS. MRI artifacts and correction strategies. *Imaging Med* 2010; 2:445–457.
  39. Katscher U, van den Berg CAT. Electric properties tomography: biochemical, physical and technical background, evaluation and clinical applications. *NMR Biomed* 2017. doi: 10.1002/nbm.3729.
  40. Katscher U, Kim DH, Seo JK. Recent progress and future challenges in MR electric properties tomography. *Comput Math Methods Med* 2013; 2013:546562.
  41. Gurler N, Ider YZ. Gradient-based electrical conductivity imaging using MR phase. *Magn Reson Med* 2017; 77: 137–150.
  42. Bulumulla SB, Lee SK, Yeo DT. Conductivity and permittivity imaging at 3.0T. *Concepts Magn Reson Part B Magn Reson Eng* 2012; 41B:13–21.
  43. Lu Y, Li B, Xu J, Yu J. Dielectric properties of human glioma and surrounding tissue. *Int J Hyperthermia* 1992; 8:755–760.
  44. Ellingson BM, Bendszus M, Boxerman J, et al. Consensus recommendations for a standardized brain tumor imaging protocol in clinical trials. *Neuro-oncology* 2015; 17:1188–1198.
  45. Savitzky A, Golay MJE. Smoothing and differentiation of data by simplified least squares procedures. *Anal Chem* 1964; 36:1627–1639.
  46. Madden MH. Comments on the Savitzky-Golay convolution method for least-squares-fit smoothing and differentiation of digital data. *Anal Chem* 1978; 50:1383–1386. doi: 10.1021/ac50031a048
  47. Katscher U, Findekle C, Voigt T. B<sub>1</sub>-based specific energy absorption rate determination for nonquadrature radiofrequency excitation. *Magn Reson Med* 2012; 68:1911–1918.
  48. Zhang X, Zhu S, He B. Imaging electric properties of biological tissues by RF field mapping in MRI. *IEEE Trans Med Imaging* 2010; 29:474–481.
  49. Zhang X, van de Moortele PF, Schmitter S, He B. Complex B<sub>1</sub> mapping and electrical properties imaging of the human brain using a 16-channel transceiver coil at 7T. *Magn Reson Med* 2013; 69:1285–1296.
  50. Zhang X, Schmitter S, van de Moortele PF, Liu J, He B. From complex B<sub>1</sub> mapping to local SAR estimation for human brain MR imaging using multi-channel transceiver coil at 7T. *IEEE Trans Med Imaging* 2013; 32:1058–1067.
  51. Hafalir FS, Oran OF, Gurler N, Ider YZ. Convection-reaction equation based magnetic resonance electrical properties tomography (cr-MREPT). *IEEE Trans Med Imaging* 2014; 33:777–793.
  52. Liu J, Zhang X, Schmitter S, van de Moortele PF, He B. Gradient-based electrical properties tomography (gEPT): a robust method for mapping electrical properties of biological tissues in vivo using magnetic resonance imaging. *Magn Reson Med* 2015; 74:634–646.
  53. Balidemaj E, van den Berg CA, Trinks J, et al. CSI-EPT: a contrast source inversion approach for improved MRI-based electric properties tomography. *IEEE Trans Med Imaging* 2015; 34:1788–1796.
  54. Liang ZP, Lauterbur PC. Principles of magnetic resonance imaging: a signal processing perspective. In Akay M ed. *IEEE Press Series in Biomedical Engineering* New York: The Institute of Electrical and Electronics Engineers, 2000; 416–422.
  55. Nishimura DG. Principles of Magnetic Resonance Imaging. Morrisville Lulu Press, 1996; 154–165.